Inorganic Chemistry

Article

pubs.acs.org/IC

Gold Network Structures in Rhombohedral and Monoclinic $Sr_2Au_6(Au,T)_3$ (T = Zn, Ga). A Transition via Relaxation

Trinath Mishra, Qisheng Lin,* and John D. Corbett*

Department of Chemistry, Iowa State University, Ames, Iowa 50011, United States

Supporting Information

ABSTRACT: Quantitative syntheses, structure determinations and interpretations, and band calculations are reported for the nonstoichiometric rhombohedral ($R\bar{3}c$) and monoclinic ($C2/c$) $Sr_2Au_6(Au_{3-x}T_x)$ (T = Zn, Ga) compounds. Several different compositions of the two Sr phases were similarly refined from single crystal X-ray diffraction data as $R\bar{3}c$: $a \approx 8.43$ Å, $c \approx 21.85$ Å, $Z = 6$ and $C2/c$: $a \approx 14.70$ Å, $b \approx 8.47$ Å, $c \approx 8.70$ Å, $\beta \approx 123.2°$, $Z = 4$. The $R\bar{3}c$ Zn phase is stable in the composition region $x \sim 2.5-2.9$ whereas its $C2/c$ neighbor is the major product at $x \sim 2.2-2.3$. Gallium versions of both were also identified. Both $R\bar{3}c$ and $C2/c$ structural types contain hexagonal-diamond-like gold superlattices stuffed with strings of interstitial Sr and disordered triangular $(Au,T)_3$ units. The latter space group is a maximal, nonisomorphic subgroup of the former, and the decrease in interstitial radius from Ba to Sr (~0.08 Å experimentally) evidently drives the symmetry reduction, relaxation, and small distortions, principally around the Sr sites. Au−Au bonding among the Au hexagons in the host lattices and with gold components in the triangular interstitials is dominant and reflected in their tight packing and short interatomic separations.

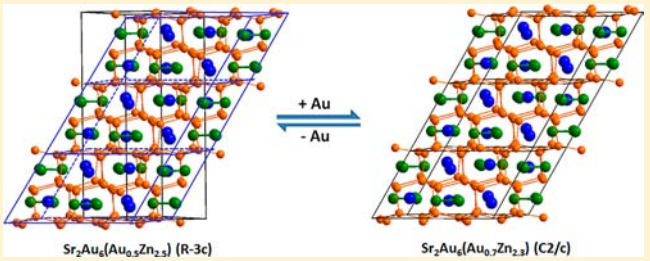

INTRODUCTION

Gold-rich intermetallic phases exhibit substantial diversities of structural motifs and bonding patterns, evidently because of the additional bonding associated with relativistic contractions and enhanced mixing of 6s orbitals with the penultimate 5d orbitals on gold.[1−6] These are reflected in smaller effective gold radii and strong covalent bonding interactions of gold with itself and with later metals in the typical high coordination environments within the A−Au−M systems we have recently investigated, for example, A = Na, K, Ca, Sr, Ba; M = Zn, Cd, Ga, In, Ge, Sn.[7−13] The recently reported rhombohedral $Ba_2Au_6(Au,T)_3$ (T = Zn, Cd, Ga, In, Sn) series exhibit an unprecedented hexagonal-diamond-like gold host lattice in which tunnels extending along the c axis are filled by ordered Ba atoms and $(Au,T)_3$ triangles.[14] The structure can be viewed as a topological atom-by-triad substitution of the AlB_2-type $BaAu_2$ ($P6/mmm$), together with the formation of delocalized bonding within the triangles and with the gold host lattice. It is of great interest to examine how the structure and bonding evolve when the Ba is replaced by smaller Sr atoms and how electronic factors matter when Zn is replaced by trivalent Ga. One germane fact here is that the corresponding binary aurides containing the smaller alkaline-earth metals Sr and Ca have $CeCu_2$-type structures ($Imma$), in contrast to the AlB_2-type $BaAu_2$ ($P6/mmm$).[15]

Here, we report the systemic investigation of the corresponding phases in the Sr−Au−T (T = Zn, Ga) systems. The syntheses and structures for both the isotypic rhombohedral phases and the new monoclinic $C2/c$ versions in the $Sr_2Au_6(Au,T)_3$ (T = Zn, Ga) systems result with the smaller Sr substituent and a higher Au contents. The crystallographic interrelationships between the two types along with a theoretical analysis of the new monoclinic derivative are presented. The neighboring $Sr_2Au_6(Au,Al)_3$ system has also recently been shown to contain similar rhombohedral and the monoclinic structures.[16]

EXPERIMENTAL SECTION

Syntheses. The surfaces of dendritic Sr pieces (99.95%, Alfa Aesar) were manually cleaned with a surgical blade before use, whereas Au particles (99.999%, BASF) and Zn shot (99.99%, Alfa Aesar) were used as received. Designed compositions were loaded into precleaned Ta tubes within an argon-filled glovebox (H_2O < 0.1 ppmv). The crimped Ta tubes were weld-sealed under argon in an arc welder and then enclosed in evacuated SiO_2 jackets (<10^{-5} Torr) to avoid their air oxidation.

At first, predetermined compositions $Sr_2Au_6(Au_{3-x}Zn_x)$ (x = 1, 2, 3) were reacted at 800 °C for ~10 h, slowly cooled to 400 °C at a rate of 2 °C/h, annealed there for two weeks, and finally quenched into water. Later on, similar samples were prepared for x = 2.2, 2.3, 2.4, 2.5 and $Sr_2Au_5Zn_4$ to check phase widths for the two different products ($R\bar{3}c$ and $C2/c$ phases). The X-ray powder pattern of the x = 3 sample showed the presence of a major fraction of the $R\bar{3}c$ phase already known with Ba,[14] and this was later verified by the structural refinement of single crystal data as well as comparisons between experimental and simulated powder pattern data. Generally new but somewhat similar patterns were found with decreasing Zn (x = 2.3, 2.2, 2.0). Overall, the appearance of new lines for compositions with x

Received: August 21, 2013
Published: November 11, 2013

   dx.doi.org/10.1021/ic402145k | Inorg. Chem. 2013, 52, 13623−13630

Table 1. Loaded Compositions, Refined Single Crystal Compositions, and Major Products, Their Estimated Yields, and Lattice Parameters and Volumes of the Rhombohedral ($R\bar{3}c$) and Monoclinic ($C2/c$) Phases $Sr_2Au_6(Au,T)_3$, (T = Zn, Ga) from Powder X-ray Diffraction Data

loaded comp	refined comp	major product + est. yields	type	a (Å)	b (Å)	c (Å)	β (deg.)	V/cell (Å^3)
$Sr_2Au_5Zn_4$	$Sr_2Au_{6.09(1)}Zn_{2.91(1)}$	60% $R\bar{3}c$ + U1[a]	$R\bar{3}c$	8.3975(4)	a	21.842(3)		1333.9(2)
$Sr_2Au_6Zn_3$	$Sr_2Au_{6.14(1)}Zn_{2.86(1)}$	90% $R\bar{3}c$ + U2	$R\bar{3}c$	8.4198(4)	a	21.895(3)		1344.2(2)
$Sr_2Au_{6.5}Zn_{2.5}$	$Sr_2Au_{6.49(1)}Zn_{2.51(1)}$	>95% $R\bar{3}c$	$R\bar{3}c$	8.4506(4)	a	21.889(3)		1353.7(2)
$Sr_2Au_{6.7}Zn_{2.3}$	$Sr_2Au_{6.71(2)}Zn_{2.29(2)}$	~60% $C2/c$ + ~40% $R\bar{3}c$	$C2/c$	14.7015(7)	8.4626(4)	8.7000(4)	123.208(4)	905.62(7)
$Sr_2Au_{6.8}Zn_{2.2}$	$Sr_2Au_{6.82(2)}Zn_{2.18(2)}$	>95% $C2/c$	$C2/c$	14.6833(7)	8.4649(4)	8.7463(4)	123.450(4)	907.04(7)
$Sr_2Au_7Zn_2$		60% $C2/c$ + 40% $SrAu_5$	$C2/c$	14.7303(7)	8.4708(4)	8.6994(4)	123.207(4)	908.23(5)
$Sr_2Au_6Ga_3$	$Sr_2Au_{6.09(2)}Ga_{2.91(2)}$	85% $R\bar{3}c$ + U3	$R\bar{3}c$	8.4334(3)	a	21.916(2)		1349.9(1)
$Sr_2Au_7Ga_2$		75% $C2/c$ + U4	$C2/c$	14.8305(8)	8.5632(4)	8.5880(5)	123.218(4)	912.43(6)

[a]U = unidentified phases.

Table 2. Crystallographic and Structural Refinement Data for Rhombohedral $Sr_2Au_6(Au,Zn)_3$ Structures

refined comp	$Sr_2Au_{6.09(1)}Zn_{2.91(1)}$	$Sr_2Au_{6.14(1)}Zn_{2.86(1)}$	$Sr_2Au_{6.49(1)}Zn_{2.51(1)}$
F.w	1564.3	1572.0	1617.0
space group, Z	$R\bar{3}c$, 6	$R\bar{3}c$, 6	$R\bar{3}c$, 6
lattice parameters, Å			
a, Å	8.3975(4)	8.4198(4)	8.4506(4)
c, Å	21.842(3)	21.895(3)	21.889(3)
V, Å^3	1333.9(2)	1344.2(2)	1353.7(2)
calc. density, g/cm^3	11.684	11.651	11.901
abs. coeff.	119.46	119.34	123.14
refl. coll./R_{int}	7521/0.0797	6793/0.0817	6216/0.0873
data/restr./para.	439/0/20	441/0/20	443/0/20
GOF	1.052	1.045	1.110
R1, wR2 for $I \geq 2\sigma(I)$	0.0216/0.0515	0.0204/0.0427	0.0269/0.0514
R1, wR2 for all data	0.0270/0.0543	0.0233/0.0437	0.0356/0.0541
ext. coeff.	0.00025(2)	0.00031(2)	0.00022(2)
residue (e Å^{-3})	2.023/−1.945	2.076/−2.351	2.552/−1.949

< 2.5 represented the splittings of peaks from the rhombohedral parent, a rather clear characteristic of modest distortions accompanying symmetry degradation, and these were established to be those of a fairly closely related monoclinic structure with similar $Sr_2Au_6(Au_{3-x}Zn_x)$ compositions. Additional peaks that appeared at x = 2.0 corresponded to those of $SrAu_5$[17] formed from an excess of gold, this being the major component at x = 1.0 (not listed).

Table 1 contains a summary of the compositions studied, the estimated product distributions and refined lattice dimensions in the mixtures therein along with compositions refined from single crystals selected from each equilibrated sample, the loaded and refined phase compositions appearing in the first two columns. All products have metallic lusters and are stable in air at room temperature for a couple of months.

To check whether isostructural phases exist with other T, the compositions $Sr_2Au_6(Au_{3-x}T_x)$ for x = 2, 3 were also investigated for T = Cd, Ga, In, Sn under the same conditions. The powder pattern of an equilibrated $Sr_2Au_6Ga_3$ composition was about 85% $R\bar{3}c$ phase (and a crystal refined as $Sr_2Au_6(Au_{0.09(2)}Ga_{2.91(2)})$ whereas that for the $Sr_2Au_6(AuGa_2)$ composition was ~75% $C2/c$ product (Table 1). However, neither these or new structure types was detected for the other elements (Cd, In, Sn). Only the Sr−Au−Zn system received more detailed investigations with respect to the monoclinic version, the composition widths of both phases, and the nature of the structural change between them.

X-ray Diffraction Studies. Phase identities and proportions were checked on the basis of powder diffraction data collected with the aid of a STADI P powder diffractometer equipped with Cu K_α radiation (λ = 1.54059 Å). Silicon (NIST 640c) was included with each sample as an internal standard. The detection limit of a second phase with this instrument and system was conservatively estimated to be about 5 vol % in equivalent scattering power. Phase identification was done with the aid of PowderCell,[18] and lattice parameters were refined with the aid of the program UnitCell[19] for data within a 2θ range of 15−70°.

Single crystals held on glass fibers were mounted on a Bruker SMART APEX CCD diffractometer equipped with Mo K_α (λ = 0.71069 Å). Data were collected with exposures of 10 s per frame over the entire reciprocal spheres, and the intensities were integrated with the SAINT program in the SMART software package.[20] Empirical absorption corrections were applied with the aid of the SADABS program.[21] The structures were solved by direct methods and subsequently refined on $|F^2|$ with a combination of least-squares refinements and difference Fourier maps.

Structure refinements for the $R\bar{3}c$ Sr phase followed those procedures described before.[14] The $C2/c$ symmetry for x = 2.3 product was first suggested by XPREP and SHELXTL 6.1.[22] Six independent sites were identified by the direct methods, and these were initially assigned as one Sr, four Au, and one Zn according to plausible Sr−Au/Zn (3.2−3.6 Å), Au−Zn (~ 2.7 Å), and Au−Au (2.8−3.1 Å) bond distances. Further refinements revealed that Zn at the 8f site had an overly small isotropic displacement parameter (0.0043 Å^2), suggesting that it could be occupied by an Au/Zn admixture instead. The isotropic value increased to 0.016 Å^2 after Au mixing was allowed, and R1 decreased from 9.11% to 7.91%. Similarly, the large (0.0297 Å^2) parameter originally refined for Au at the 4e site decreased to 0.0138 Å^2 when Au/Zn mixing was allowed, and R1 further decreased to 6.23%. Full occupancy was suggested for the remaining sites because their deviations from 100% occupancy were <2σ. Final least-squares refinements, with anisotropic displacement parameters and a secondary extinction correction, yielded $Sr_2Au_{6.71(2)}Zn_{2.29(2)}$ at R1 = 4.1%, wR2 = 7.86%, and GOF = 1.080 for 54 parameters refined from 1323 observed independent data. Single crystal data for the rhombohedral and monoclinic phases are listed in Tables 2 and 3, respectively, whereas the positional data from all of these are in Table 4. Supporting Information, Tables S1 and S2

dx.doi.org/10.1021/ic402145k | Inorg. Chem. 2013, 52, 13623−13630

Table 3. Crystallographic and Structural Refinement Data for Monoclinic $Sr_2Au_6(Au,Zn)_3$ Structures

refined composition	$Sr_2Au_{6.71(2)}Zn_{2.29(2)}$	$Sr_2A_{u6.82(2)}Zn_{2.18(2)}$
F.w.	1646.2	1660.4
space group, Z	$C2/c$, 4	$C2/c$, 4
lattice parameters		
a, Å	14.7015(7)	14.6833(7)
b, Å	8.4626(4)	8.4649(4)
c, Å	8.7000(4)	8.7463(4)
β	123.208(4)°	123.450(4)°
V, Å^3	905.62(7)	907.04(7)
calc. density, g cm^{-3}	12.074	12.159
abs. coeff. (mm^{-1})	125.73	126.98
refl. coll./R_{int}	9514/0.0793	9496/0.0849
data/restr./para.	1323/0/54	1323/0/54
GOF	1.080	1.126
R1, wR2 for $I \geq 2\sigma(I)$	0.0410/0.0786	0.0465/0.1061
R1, wR2 for all data	0.0539/0.0828	0.0554/0.1093
ext. coeff.	0.00018(2)	0.00042(5)
residues (e Å^{-3})	3.330/−3.095	5.947/−3.850

contain the structural and refinement data for rhombohedral $Sr_2Au_6(Au_{0.09(2)}Ga_{2.91(2)})$. Powder pattern comparisons between those for bulk products and from single crystal analyses for various $Sr_2Au_6(Au,T)_3$ (T = Zn, Ga) samples are given in Figure 1, Supporting Information, Figures S1, S2, and S3.

Electronic Structure Calculations. Tight binding calculations were performed according to the linear-muffin-tin-orbital (LMTO) method in the atomic sphere approximation (ASA)[23,24] to gain better understanding regarding the bonding in the new monoclinic phase, the rhombohedral structure having been so considered earlier for the Ba analogues.[14] An idealized monoclinic $C2/c$ model for $Sr_2Au_7Zn_2$ is described later. No additional empty spheres were necessary beyond those described automatically, subject to a 16% overlap restriction between atom-centered spheres. All spheres had reasonable radii (Å): Sr: 2.17, Au1: 1.59, Au2: 1.56, Au3: 1.52, Au4: 1.56, and Zn: 1.45, respectively. Basis sets of 4d/5s/(5p) for Sr, 5d/(5f)/6s/6p for Au, and (3d)/4s/4p/for Zn (downfolded orbitals in parentheses) were employed, and scalar relativistic corrections were included in the calculations. The band structure was sampled at 12 × 12 × 12 k points in the irreducible wedge of the Brillouin zone. Crystal orbital Hamilton population (COHP) analyses[25] were also undertaken.

RESULTS AND DISCUSSION

Phase Distributions. The powder patterns for $Sr_2Au_6(Au_{3-x}Zn_x)$ samples with the nominal compositions x = 2.50 (rhombohedral $R\bar{3}c$, top) and x = 2.20 (monoclinic $C2/c$, bottom) are shown as black curves in Figure 1 along with the powder patterns (red) calculated from refined single crystals data for the respective compositions. The close agreement for each pair indicates that the synthesized products contain ≥95% of the desired phases. Such close agreements verify the correctness of the refined single crystal compositions for the two samples considerably better than could be achieved from microprobe, EDX, and so forth analyses. The reaction with x = 3 also produced ∼90% of the $R\bar{3}c$ phase whereas reactions with x = 2.3 and $Sr_2Au_5Zn_4$ resulted in multiphased patterns (Supporting Information, Figure S1). The single crystal compositions for the three $R\bar{3}c$-based samples (see Table 1) put the breadth of this phase at between ∼97 and <84% Zn at 400 °C, whereas the overall lattice dimension ranges are well established by the original powder data, Table 1.

Table 4. Atomic Coordinates (×10^4) and Equivalent Isotropic Displacement Parameters (Å^2 × 10^4) for the Rhombohedral (R) and Monoclinic (Mc) Phases of $Sr_2Au_6(Au,Zn)_3$

atom	Wyck.	symm.	x	y	z	U_{eq}	Au/Zn Occ. (%)
			$Sr_2Au_{6.09(1)}Zn_{2.91(1)}$ (R)				
Sr	12c	3.	0	0	924(1)	9(1)	
Au	36f	1	3451(1)	361(1)	165(1)	14(1)	
M[a]	18e	0.2	1921(2)	0	1/4	12(1)	3.1/96.9(5)
			$Sr_2Au_{6.14(1)}Zn_{2.86(1)}$ (R)				
Sr	12c	3.	0	0	924(1)	11(1)	
Au	36f	1	3460(1)	371(1)	164(1)	11(1)	
M	18e	0.2	1907(2)	0	1/4	11(1)	4.8/95.2(5)
			$Sr_2Au_{6.49(1)}Zn_{2.51(1)}$ (R)				
Sr	12c	3.	0	0	936(1)	14(1)	
Au	36f	1	3432(1)	357(1)	163(1)	15(1)	
M	18e	0.2	1860(2)	0	1/4	13(1)	16.3/83.7(5)
			$Sr_2Au_{6.71(2)}Zn_{2.29(2)}$ (Mc)				
Sr	8f	1	1526(2)	2457(2)	2173(2)	13(1)	
Au1	8f	1	1005(1)	8815(1)	494(1)	16(1)	
Au2	8f	1	2185(1)	771(1)	9523(1)	13(1)	
Au3	8f	1	789(1)	5564(1)	9506(1)	13(1)	
M1	8f	1	946(2)	6570(2)	2499(2)	14(1)	10.5/89.5(7)
M2	4e	2	0	9293(2)	1/4	12(1)	50/50(1)
			$Sr_2Au_{6.82(2)}Zn_{2.18(2)}$ (Mc)				
Sr	8f	1	1503(2)	2429(2)	2178(3)	12(1)	
Au1	8f	1	1043(1)	8783(1)	503(1)	14(1)	
Au2	8f	1	2201(1)	782(1)	9530(1)	12(1)	
Au3	8f	1	781(1)	5540(1)	9501(1)	12(1)	
M1	8f	1	957(2)	6570(2)	2496(3)	12(1)	5.1/94.9(9)
M2	4e	2	0	9276(2)	1/4	10(1)	70/30(1)

[a]M = Au/Zn.

dx.doi.org/10.1021/ic402145k | Inorg. Chem. 2013, 52, 13623−13630

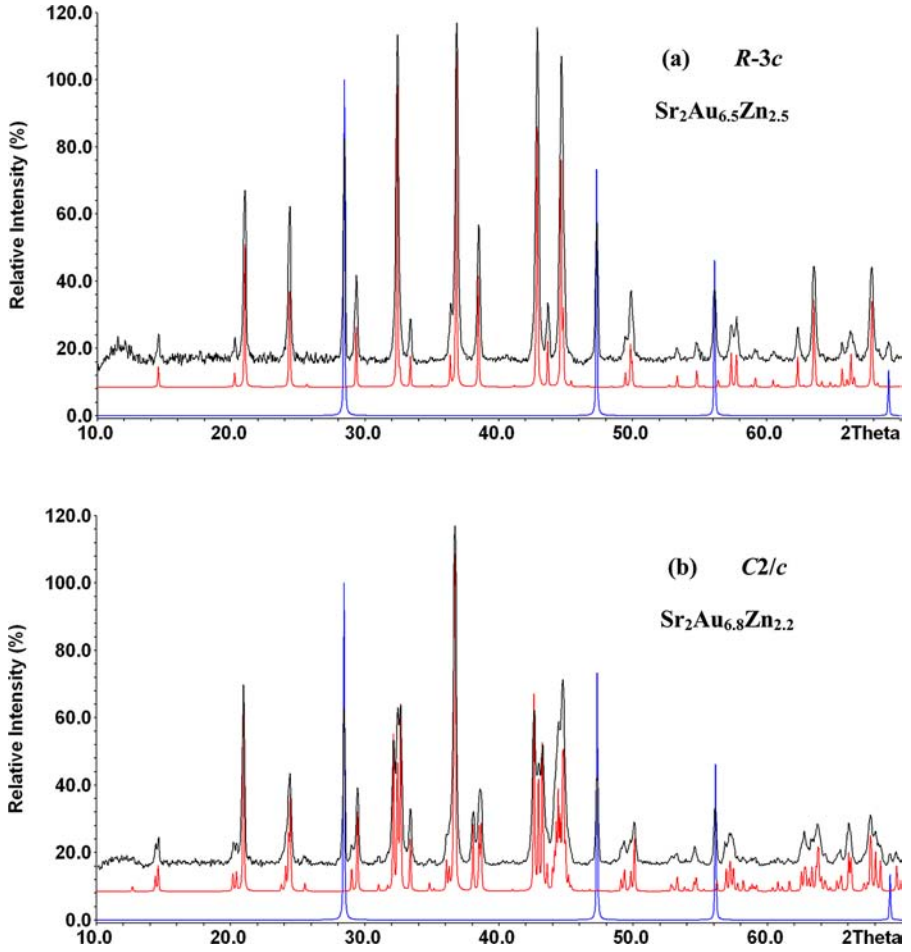

Figure 1. Powder patterns of different loaded products (black) and calculated patterns derived from single crystal data (red) for the rhombohedral $R\bar{3}c$ (a) and the monoclinic $C2/c$ (b) structures in $Sr_2Au_6(Au,Zn)_3$ system. Blue curves are patterns of the Si standard.

In contrast, the reaction with more gold, $x = 2.2$, produced the new $C2/c$ phase in ≥95% yield, but reactions with $x = 2.0$ yielded mixed products (Supporting Information, Figure S2). These more scattered results indicate that the monoclinic phase, now with two mixed Au/Zn positions, is homogeneous between 76% and somewhere below 72% Zn.

The range of valence electrons counts per atom (e/a) for the $R\bar{3}c$ zinc phase is narrow, within 1.41−1.45 considering Au 5d[10] states as core, appreciably less than in the corresponding Ba system, 1.27−1.42;[14] similarly, e/a values for the $C2/c$ zinc phase span only 1.37−1.39. The e/a datum for the gallium-richer $R\bar{3}c$ analogue analyzed is 1.71, larger than that for Ba parallel compound.[14]

Structural Descriptions. The single crystal X-ray diffraction results (Tables 2−4) established that the first three refined compositions, $Sr_2Au_6(Au_{0.09(1)}Zn_{2.91(1)})$, $Sr_2Au_6(Au_{0.14(1)}Zn_{2.86(1)})$, and $Sr_2Au_6(Au_{0.49(1)}Zn_{2.51(1)})$, are isostructural with the rhombohedral ($R\bar{3}c$) $Ba_2Au_6(Au_{\sim 2.06}Sn_{\sim 0.94})$[14] (Pearson symbol *hR*66), whereas the two gold-richer products $Sr_2Au_6(Au_{0.71(2)}Zn_{2.29(2)})$ and $Sr_2Au_6(Au_{0.82(2)}Zn_{2.18(2)})$ exhibit a new monoclinic ($C2/c$) structure type (Pearson symbol *mS*44). The unit cell of the former is seen in Figure 2 as a hexagonal-diamond-like host lattice of gold, together with interstitial Sr atoms (blue) and disordered equilateral $(Au/Zn)_3$ triangles (green), namely, $Au_{0.49(1)}Zn_{2.51(1)}$ in the tunnels viewed along *c*. The two interstitials, in an ordered 2:1 proportion, are tightly bound with the gold host lattice, as indicated by the −ICOHP data (below). The total unit cell contents can be further described in

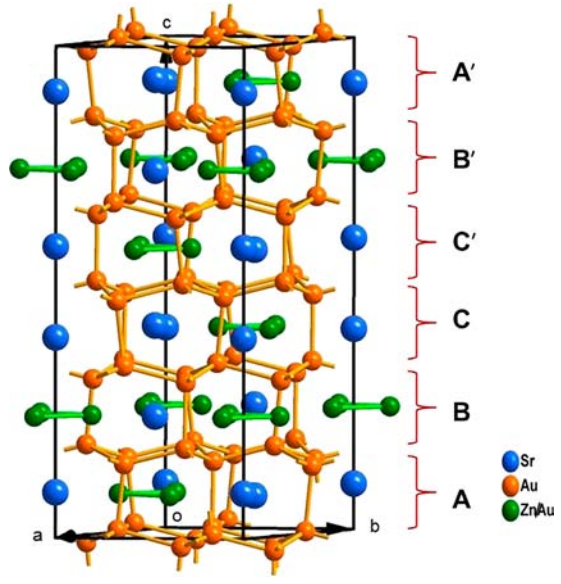

Figure 2. Rhombohedral phase ($R\bar{3}c$) $Sr_2Au_6(Au,Zn)_3$, with a hexagonal-diamond-like gold lattice stuffed with interstitial Sr (blue) and triangular units M_3 (green). A, B, C, C′, B′, and A′ mark the relative stacking of layers along the *c* axis.

dx.doi.org/10.1021/ic402145k | *Inorg. Chem.* 2013, 52, 13623−13630

terms of regular stacking of six slabs of puckered gold layers that sandwich Sr and $(Au,Zn)_3$ interstitials along c according to the relative positional sequences A, B, C plus the inverted C′, B′, A′. (More details in reference 14.) All puckered gold layers are symmetry-equivalent, each an ordered net of two differently sized six-membered gold rings that share edges, and the pairs of six-membered rings above and below each interstitial are further interconnected along $\pm c$ by means of intermediate Au−Au bonds (∼ 2.96 Å) or pillars.

Figure 3(a) shows the environments of the interstitial Sr and $(Au,T)_3$ triangles. Each is surrounded by a cage of Au atoms, with C_3 symmetry about Sr and D_3 around the larger M_3 members. All of the Sr atoms in the present phases have 9 or 10 nearest Au neighbors below 4.0 Å. (The remainder are Zn, in contrast to members of the $R\bar{3}c$ Ba family in which half of the eight structurally characterized variations have 12 nearest neighbor Au about Ba.) Regardless, each interstitial cage is generated by two differently sized six-membered rings of Au puckered in trans-configurations. The top smaller ring above Sr consists of two sets of three equal and short Au−Au distances (2.852(1) Å), and all internal angles within the ring are equal, 113.99(1)°. In contrast, the bottom large ring around Sr contains three longest (3.082(1) Å) and three shortest (2.852(1) Å) Au−Au distances, alternating each other as it accommodates to the larger triangular insert; thus there are two groups of internal bond angles in this ring (Figure 3a and Supporting Information, Figure S4). The bottom ring of Sr is shared with the M_3 interstitial below it, as the top ring of M_3. Noteworthy is that the bottom ring around M_3 is symmetry equivalent with its top ring, by a rotation of 60°.

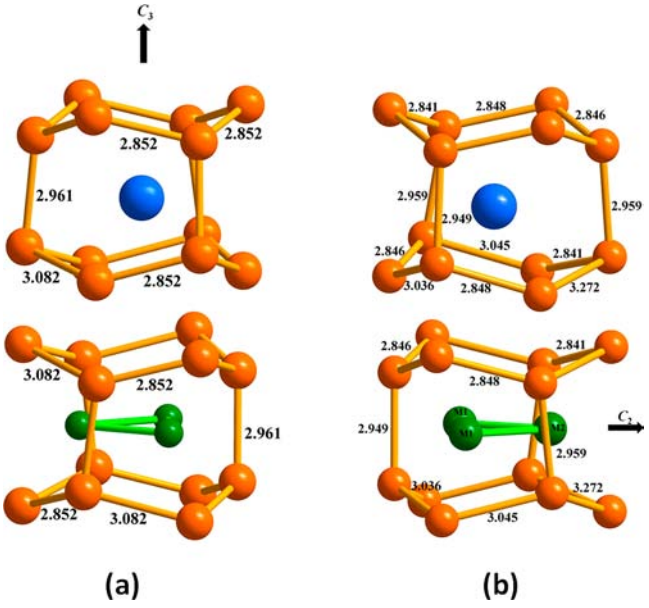

Figure 3. (a) Gold environments of Sr (blue) and equilateral M_3 (green) interstitials in the trigonal $Sr_2Au_{6.49(1)}Zn_{2.51(1)}$ ($R\bar{3}c$). Both lie on a vertical 3-fold axis, and the equilateral triangle also has three 2-fold axes through the atoms. (b) The environments of interstitial Sr and triangular M'_3 in the monoclinic ($C2/c$) structure, $Sr_2Au_6(Au_{0.71(2)}Zn_{2.29(2)})$. The unique M_2 atom lies on a 2-fold axis. The middle two Au layers are the same in the actual structures.

The new $C2/c$ phase has the same formula but somewhat higher gold contents in the M_3 units, $Sr_2Au_6(Au_{0.71(2)}Zn_{2.29(2)})$ in the present case, but these seemingly require only modest geometric changes to generate a monoclinic lattice. Although the space group $C2/c$ is one of the maximal subgroups of the parent $R\bar{3}c$ group through a t3 operation, the relationship between these two lattices is not as straightforward as might be imagined because of the involvement of nonisomorphic transition(s) in later steps. According to group-subgroup theorem, a t3 operation can only change the hexagonal $R\bar{3}c$ lattice to a monoclinic $C2/c$ lattice with dimensions of $(-1/3a + 1/3b - 2/3c, -a - b, c)$ or its equivalent. At least two other i3 operations, that is, $(3a, b, a + c)$ and $(1/3a, b, c)$, must also be taken to get to the present $C2/c$ lattice thereafter. In the $C2/c$ structure, isosceles triangles M'_3 ($M' = (M1)_2M2$) defined by mixed and disordered M1 (8*f*) and M2 (4*e*) sites now replace the former equilateral M_3 triangles (M = Au/Zn), retaining a single 2-fold axis though the M2 site. Even though considerable descent in symmetry is involved, the same basic structure remains, the most obvious distortions being in the environment of the smaller Sr atoms (Figure 3b), which are less strongly bonded to the Au lattice than the triangular units (below).

Figure 4 is a conventional (101) view of the monoclinic cell for the $Sr_2Au_6(Au_{0.71(2)}Zn_{2.29(2)})$. Of particular note is the fact that the "...Sr−M_3−Sr..." sequence of interstitials in the vertical chains are only slightly perturbed. (The interstitial sequences are somewhat obscured in Figure 4 by the double columns generated by the C-centering; see more below.) Some recovery from the poor packing is achieved by increased binding of the Au-richer and somewhat larger Au/Zn units as M'_3 units, but a volume increase of 0.20% is incurred on changes of neighboring triangle compositions ($Au_{0.49}Zn_{2.51}$ and $Au_{0.71}Zn_{2.29}$, Table 1). Displacements according to the $\beta - 90° = 33.2°$ angle basically

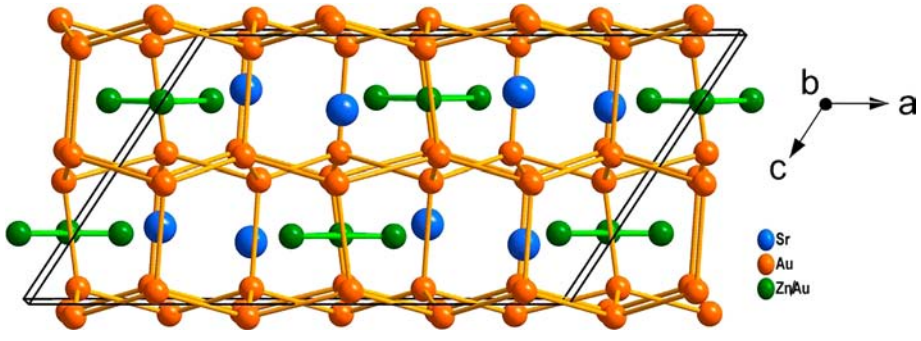

Figure 4. (101) view of the monoclinic ($C2/c$) $Sr_2Au_6(Au_{0.71(2)}Zn_{2.29(2)})$, a slightly distorted substructure of the rhombohedral parent. The M'_3 units (green) are now isosceles triangles with a 58.9° angle on the 2-fold axis normal to the page. Notice the persistence of roughly vertical Sr−M′−Sr chains from the parent compound.

dx.doi.org/10.1021/ic402145k | *Inorg. Chem.* 2013, 52, 13623−13630

establish the repeat distances between vertical interstitial chains along *a*, Figure 4. In some more detail, the M1 (8*f*) site at this composition is dominated by ~90% Zn but the M2 (4*e*) position (on the remaining 2-fold axis) is substantially equiatomic Au and Zn. The unique angle in the isosceles triangle is 58.9(1)°, and the opposed edge is 0.09 Å shorter. The hexagonal-diamond-like gold host lattice, formerly generated by 36*f* sites, is now defined by Au1, Au2, Au3, each in an 8*f* Wyckoff site (Z = 4). All puckered gold layers again have two differently sized but now lower symmetry six-member Au rings that share edges (Supporting Information, Figure S5). Notwithstanding the structural changes, the first nine nearest-neighbor Sr–Au contacts have basically the same distance range, 3.23 to 3.34 (±0.01) Å, in both the $R\bar{3}c$ and $C2/c$ structures when compared at the most similar Zn contents. On the other hand, the same comparisons for Sr versus Ba for the first nine contacts in $R\bar{3}c$ do matter, as would be expected, but only by 0.08 Å. The last contrasts with a 10-coordinate difference of ~0.16 Å in their general (Shannon) crystal radii,[26] which affords a useful observation about size differences in intermetallic bonding in the present phases. The Ba member achieves 12 nearest-neighbor Au contacts in $Ba_2Au_6(Au_{1.11}Zn_{1.89})$, but distances to two mixed (Zn, Au) sites in the triangular interstitials intrude for the 11th and a more distant 12th Sr contacts (Supporting Information, cif files). Gallium is not included in this comparison in view of the appreciable change in valence electron count and distances observed for Ga in the Ba systems.[14]

Visualizing the net changes that take place in the Sr chemistry needs the better definition designed into Figure 5. For straightforward comparisons, the (a)-(c) and (b)-(d) pairs of the respective rhombohedral and monoclinic cells are shown with exactly the same contents and similar projections. Three ideal (unperturbed) monoclinic unit cells are projected onto the trigonal lattices (black boundaries) in (a), whereas the equivalent refined monoclinic result is illustrated in (c). As shown, the local structure changes turn out to be qualitatively small, suggesting that the symmetry reduction may afford a simple means to relieve the strain (poorer packing) originating with the undersized Sr cation relative to the better-ordered Ba phases. The dashed red line in (c) is used to guide the viewer along the less constrained Sr and $(M')_3$ positions along the *c* direction, in contrast to the regularity along the 3-fold axes in (a). The comparisons (b) and (d) relate the parallel $R\bar{3}c$ and $C2/c$ placements of the chains of blue Sr pairs and triangular green $(M')_3$ interstitials in the gold lattices along the (001) and (011) directions of (a) and (b), respectively. Only the 2-fold axes parallel to *b* are important in the (011) projection in (d). These last comparisons involve relatively long intervals between successive triangular M'_3 units in (a) and (c), 50% of each figure height. A lack of trigonal symmetry in M'_3 and small irregularities among the Sr positions can be seen in (d), even on this scale. The more or less centered Sr atoms project a larger image in the monoclinic projection, whereas the fractional positional errors of most atoms in the monoclinic X-ray diffraction refinement were about double those in $R\bar{3}c$. In other words, the lower symmetry monoclinic version is "more relaxed". (In a related matter, the more similar wobbles in the two gold networks evident in (c) versus (d) originate more from rather parallel effects that two differently sized interstitials have on cavity sizes through successive Au networks.)

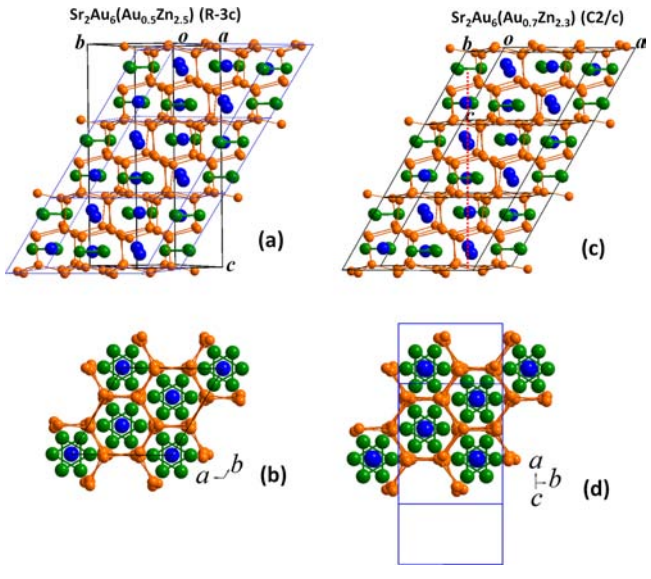

Figure 5. Structural comparisons between the trigonal $Sr_2Au_6(Au_{1.49(1)}Zn_{2.51(1)})$ ($R\bar{3}c$), (a)–(b), and the monoclinic $Sr_2Au_6(Au_{0.71}Zn_{2.29(2)})$ ($C2/c$), (c)–(d). For straightforward comparison, (a)–(c) and (b)–(d) pairs are shown with exactly the same contents and similar projections. In (a), three monoclinic unit cell frameworks as in (c) are overlaid on the trigonal structure. A dashed red line in (c) is used to guide the wobble of Sr atoms along the *c* direction, in contrast to the linear projections in (a) and (b). Note that the larger Sr atoms (blue) exhibit reduced order in (d).

Electronic Structure Calculations. Considering the two mixed triangular interstitial sites as fully occupied by the predominant component yields a useful hypothetical monoclinic $Sr_2Au_6(AuZn_2)$ model (*vec* = 85e, including Au d^{10}) in place of $Sr_2Au_6(Au_{0.82}Zn_{2.18})$. In this way, the M1 (8*f*) and M2 (4*e*) are assigned as Zn and Au respectively. The model rhombohedral Ba phase was previously described similarly.[14]

Bond length ranges and –ICOHP values for this monoclinic model $Sr_2Au_{6(}(Au_1Zn_2)$ are listed in the Table 5, and the calculated total and partial orbital densities-of-states (DOS) and the various crystal orbital Hamilton populations (COHP[25]) in this model are illustrated in Figure 6. The presence of sizable DOS bands at the Fermi energy indicates that the monoclinic model would have a metallic character. The individual orbital DOS show the dominance of split Au 5d states, with some 6s mixing as well in the lower bonding region, whereas some 6p states extend above E_F. Substantial interactions among a group of Sr 5s, 4d states with Au 5d and Zn 4s, 4p components lie in the lower part of the orbital DOS and in the –COHP data, all below –4 eV. The Sr 4d (5s)–Au 5d portion above about –6 eV reflects some sort of "back bonding" into cation states, simply put. The negative "filled band" nature of the Au–Au bonding around –3.5 eV is relatively small when compared with the full expanse of the Au–Au –COHP band at lower energies and, indeed, a similarly small effect is found around –3 eV for the comparable rhombohedral $Ba_2Au_6(AuZn_2)$[14] when allowance is made for the very different plotting scales. The relative contributions are in fact largely similar to those seen in other gold phases.

The overall trends, particularly in the Au–Au shell bonding over the series $Ba_2Au_6(An/Zn)_2$ ($R\bar{3}c$) through the corresponding $Sr_2Au_6(An/Zn)_2$ ($R\bar{3}c$) to monoclinic $Sr_2Au_6(An/Zn)_2$ ($C2/c$), are also relatively smooth when compared at similar Zn proportions in the other interstitial site, that is, 2.60/2.51/2.29 out of 3.00, respectively. The corresponding Au–Au

dx.doi.org/10.1021/ic402145k | Inorg. Chem. 2013, 52, 13623–13630

Table 5. Bond Lengths and −ICOHP Values for the Ideal Monoclinic $Sr_2Au_7Zn_2$

bond[a]	length (Å)	−ICOHP (eV/per bond)	*n*/cell	−ICOHP (eV/cell)	%
$(Au)_H$−$(Au)_H$	2.836−3.315	1.03	48	54.2	25.0
$(Au)_H$−$(Au)_T$	2.687−2.890	1.40	24	33.6	15.5
$(Au)_H$−Zn	2.607−2.814	1.02	72	73.4	33.8
$(Au)_T$−Zn	2.693	1.05	8	8.40	3.9
Zn−Zn	2.799	0.56	4	2.24	1.0
Sr−$(Au)_H$	3.217−3.745	0.39	96	37.4	17.2
Sr−$(Au)_T$	3.583−3.699	0.22	16	3.5	1.6
Sr−Zn	3.632−3.773	0.14	32	4.5	2.1

[a] $(Au)_H$−Au_6 occur in hexagons, $(Au)_T$−Au are in the triangular units in the $Sr_2Au_7Zn_2$ model.

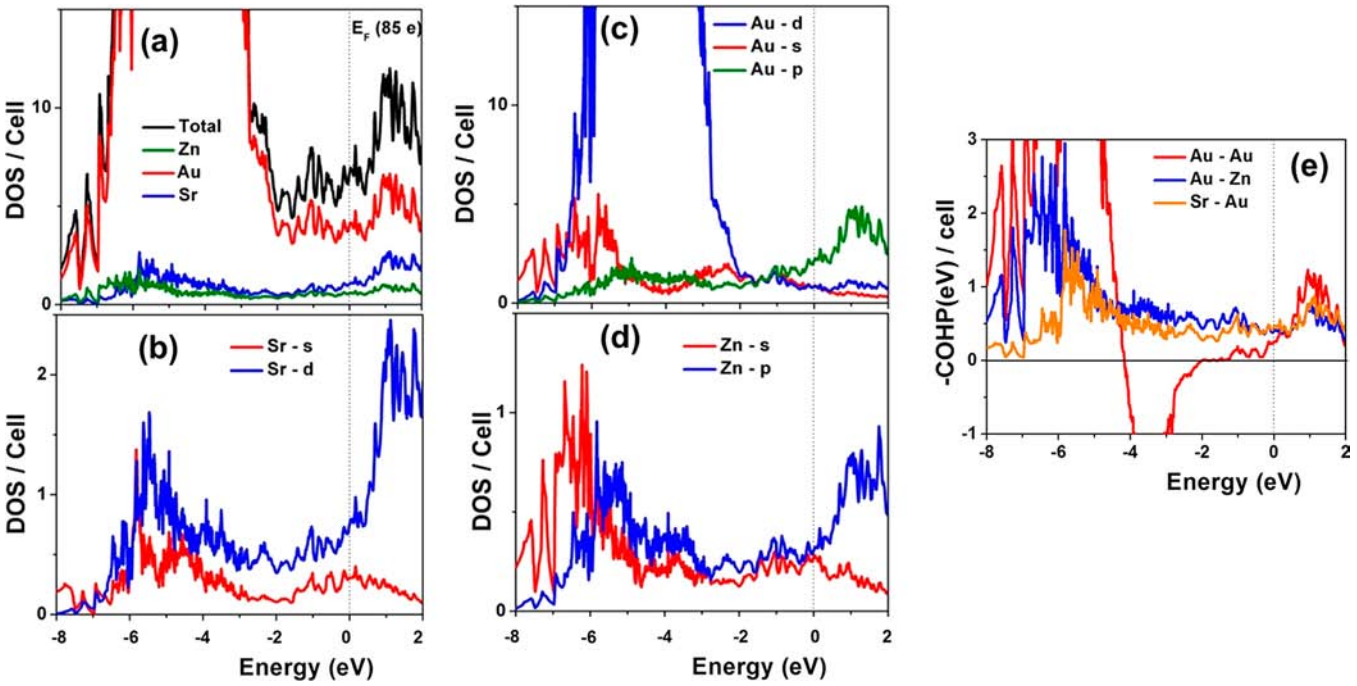

Figure 6. LMTO-ASA calculations for the ideal $C2/c$−$Sr_2Au_7Zn_2$ considering Zn 3d as a core. (a) Densities-of-states (DOS) for different atom types. Partial projections of orbital components of (b) Sr: 5s,4d; (c) Au: 5d,6s,6p; (d) Zn: 4s, 4p; (e) COHP curves for: Au−Au (red), Au−Zn (blue), Sr−Au (orange). Zn−Zn and Sr−Zn data are not significant.

distance ranges therein are 2.92−3.12, 2.85−3.08, and 2.61−3.04 Å, reflecting the introduction of the smaller cation, and then the transition to a somewhat expanded monoclinic cell with some small increases in disorder or less tight bonding.

Some generalities about the sources of bonding in the model monoclinic phase are revealed in Table 5 in terms of bond distance ranges and average −ICOHP values, using Au_H and Au_T to distinguish hexagonal network from the triangular interstitial gold functions. The bond type with highest population per bond mol, Au_H−Au_T at 1.40 eV mol^{-1}, involves the unique interactions of the isolated Au-richer M2, the vertex of the isosceles triangle, with the hexagonal Au sheath. But there are three times as many Au_H−Zn interactions with a somewhat lesser −ICOHP (1.04), the latter defining the unique edge of this triangle, and these sum up to nearly 34% of the total −ICOHP per cell; some of these are also the shortest bonds in the compound, 3.607 Å. The somewhat less frequent Au_H−Au_H interactions per cell account for 25% of the total in the structure. Interestingly, the most frequent contacts per cell, Sr−Au_H (Figure 3), are in third place, with 17% of the total −ICOHP. This complex structure exhibits a considerable range of interactions to define its stability, and yet at this point we have little idea of what the principal alternative products are. Overall, an increase in interstitial gold content in its many roles appears to be significant in the transformation from the high symmetry rhombohedral to this novel "relaxed" monoclinic version.

CONCLUSIONS

The present study gives a first look at the in-principle "simple" effects that a switch of a cation to its "simple" next smaller congener can have on the somewhat complex solid state chemistry for only two of the five examples of T in $Ba_2Au_6(Au,T)_3$ systems. Substitutions of Eu or, perhaps, Tb in the cation role are presumably good possibilities as well. The highly interdependent, yet basically unpredictable, roles that various components can play in determining stability or instability give the experimentalist a great advantage. And what even larger and impressive products are possible?

ASSOCIATED CONTENT

Supporting Information

The observed and calculated X-ray powder diffraction patterns for $R\bar{3}c$ and $C2/c$ phases of $Sr_2Au_6(Au,T)_3$ (T = Zn, Ga)

dx.doi.org/10.1021/ic402145k | Inorg. Chem. 2013, 52, 13623−13630

systems (Figures S1, S2, S3). Projection of single puckered layers of Au atoms in the $R\bar{3}c$ and $C2/c$ phases of $Sr_2Au_6(Au,Zn)_3$ (Figures S4, S5). Crystal and refinement data for the $R\bar{3}c$ phase in $Sr_2Au_6(Au,Ga)_3$ system (Tables S1, S2). Single-crystal X-ray crystallographic information files (CIF) for all crystals so studied. This material is available free of charge via the Internet at http://pubs.acs.org.

AUTHOR INFORMATION

Corresponding Authors

*E-mail: qslin@ameslab.gov (Q.L.).
*E-mail: jcorbett@iastate.edu (J.D.C.).

Notes

The authors declare no competing financial interest.

ACKNOWLEDGMENTS

This research is supported by the U.S. National Science Foundation, Solid State Chemistry, via Grant DMR-0853732. All the work was performed in the facilities of the Ames Laboratory, U.S. Department of Energy. Q.L. is partially supported by DOE BES (data analyses and writing).

REFERENCES

(1) Li, B.; Kim, S.-J.; Miller, G. J.; Corbett, J. D. *Inorg. Chem.* **2009**, *48*, 6573.
(2) Corbett, J. D. *Inorg. Chem.* **2010**, *49*, 13.
(3) Wang, F.; Pearson, K. N.; Straszheim, W. E.; Miller, G. J. *Chem. Mater.* **2010**, *22*, 1798.
(4) Miao, M. S.; Kurzman, J. A.; Mamen, N.; Narasimhan, S.; Seshadri, R. *Inorg. Chem.* **2012**, *51*, 7569.
(5) (a) Pyykkö, P. *Chem. Rev.* **1988**, *88*, 563. (b) Pyykkö, P. *Angew. Chem., Int. Ed.* **2004**, *43*, 4412.
(6) Li, B.; Corbett, J. D. *J. Am. Chem. Soc.* **2006**, *128*, 12392.
(7) Lin, Q.; Corbett, J. D. *Inorg. Chem.* **2007**, *46*, 8722.
(8) Dai, J.-C.; Corbett, J. D. *Inorg. Chem.* **2007**, *46*, 4592.
(9) Lin, Q.; Corbett, J. D. *Inorg. Chem.* **2011**, *50*, 1808.
(10) Lin, Q.; Corbett, J. D. *Inorg. Chem.* **2011**, *50*, 11091.
(11) Gupta, S.; Corbett, J. D. *Inorg. Chem.* **2012**, *51*, 2247.
(12) Samal, S. L.; Lin, Q.; Corbett, J. D. *Inorg. Chem.* **2012**, *51*, 9395.
(13) (a) Smetana, V.; Corbett, J. D.; Miller, G. J. *Inorg. Chem.* **2012**, *51*, 1695. (b) Smetana, V.; Corbett, J. D.; Miller, G. J. *J. Solid State Chem.* **2013**, *207*, 21.
(14) Lin, Q.; Mishra, T.; Corbett, J. D. *J. Am. Chem. Soc.* **2013**, *135*, 11023.
(15) Villars, P.; Calvert, L. D. *Pearson's Handbook of Crystallographic Data for Intermetallic Phases*; American Society of Metals: Materials Park, OH, 1991.
(16) Palasyuk, A.; Miller, G. J. to be submitted.
(17) Palenzona, A. *Atti Accad. Nazionale Lincei, Cl. Fis., Mat. Nat., Rend.* **1967**, *42*, 504.
(18) Kraus, W.; Nolze, G. In *Powder Cell for Windows*; http://www.bam.de/de/service/publikationen/powder_cell.htm.
(19) Holland, T. J. B.; Redfer, S. A. T. *Mineral. Mag.* **1997**, *61*, 65.
(20) *SMART*; Bruker AXS, Inc.; Madison, WI, 1996.
(21) Blessing, R. H. *Acta Crystallogr., Sect. A* **1995**, *51*, 33.
(22) *SHELXTL*; BrukerAXS, Inc.: Madison, WI, 2000.
(23) Krier, G.; Jepsen, O.; Burkhardt, A.; Andersen, O. K. *TB-LMTO-ASA Program*, version 4.7; Max-Planck-Institut für Festkörperforschung: Stuttgart, Germany, 1995.
(24) Jepsen, O.; Andersen, O. K. *Z. Phys. B* **1995**, *97*, 35.
(25) Dronskowski, R.; Blöchl, P. E. *J. Phys. Chem.* **1993**, *97*, 8617.
(26) Shannon, R. D. *Acta Crystallogr., Sect. A* **1976**, 751.